

# WISE-FUSE: Efficient Whole Slide Image Encoding via Coarse-to-Fine Patch Selection with VLM and LLM Knowledge Fusion

Yonghan Shin, SeungKyu Kim, Won-Ki Jeong<sup>†</sup>

Department of Computer Science and Engineering, College of Informatics, Korea University, Republic of Korea  
{dydgks592,ksk8804,wkjeong}@korea.ac.kr

## Abstract

Whole slide images (WSIs) in computational pathology (CPath) pose a major computational challenge due to their gigapixel scale, often requiring the processing of tens to hundreds of thousands of high-resolution patches per slide. This results in prohibitive encoding costs, with preprocessing and training times extending to days or even weeks—making WSI encoding the most significant bottleneck in real-world deployment. In this work, we propose WISE-FUSE, an adaptive WSI encoding framework that leverages pathology-domain vision-language models and large language models to address this challenge by selectively processing diagnostically relevant regions. WISE-FUSE first computes similarity scores between low-resolution patches and class-specific textual descriptions using a knowledge distillation mechanism that preserves fine-grained diagnostic features. Based on these similarity scores, we select a small subset of informative regions for the target task, which quickly eliminates irrelevant patches at the coarse level. The corresponding high-resolution patches are then selectively encoded and fused with textual embeddings to reinforce diagnostic context. Extensive experiments demonstrate that WISE-FUSE reduces WSI encoding time by over threefold while achieving diagnostic performance comparable to or surpassing that of exhaustive patch processing, offering a scalable and practical solution for CPath.

## Introduction

With the advent of advances in digital imaging and artificial intelligence (AI), analyzing pathological data using computational methods, i.e., computational pathology (CPath), plays a vital role in accurate disease diagnosis and treatment planning. For the effective implementation of CPath, high-resolution whole slide images (WSIs) are essential, as they provide a hierarchical representation of tissue at multiple magnifications, where lower magnifications (e.g., 5 $\times$ ) capture tissue-level architecture and higher magnifications (e.g., 20 $\times$ ) reveal detailed cellular morphology.

Owing to the gigapixel scale of WSIs, it is standard practice to partition each WSI into thousands to hundreds of thousands of small image patches at various magnification levels, and to employ a multiple instance learning (MIL) framework in which each patch is treated as an individual

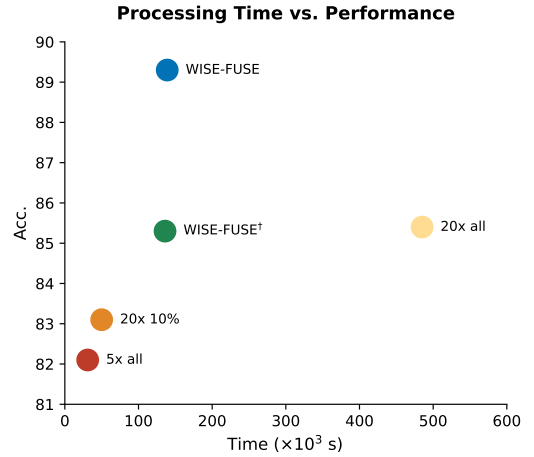


Figure 1: Comparison of classification accuracy vs. WSI processing time for TCGA-BRCA cancer subtyping. The plot shows that WISE-FUSE achieves higher classification accuracy ( $>89$ ) while reducing processing time by 1/3 compared to using all high-resolution patches (20 $\times$  all).

instance and the entire slide is considered a bag (Ilse, Tomczak, and Welling 2018). However, incorporating the entire set of patches in the MIL framework is not only computationally intensive but also suboptimal for performance. Dong et al. (2025) observed that the majority of patches contribute minimally to the final prediction and may even introduce noise. Furthermore, we found that a substantial portion of computational time is consumed by patch-level image encoding in the MIL framework. For instance, encoding all patches from the TCGA-NSCLC dataset (3129 WSIs, total size 1150 GB) required approximately two weeks while training a model took only less than an hour on an NVIDIA RTX 4090 GPU, making patch encoding a significant bottleneck in building AI models for CPath.

Several prior studies have sought to reduce computational cost in WSI analysis by employing Region-of-Interest (ROI) detection and patch selection strategies. Early work by Nugaliyadde et al. (Nugaliyadde et al. 2020) and Hossain et al. (Hossain et al. 2023) introduced using a pre-trained ROI detector, which requires substantial annotations

and supervised training. Recent methods such as SMT (Yu et al. 2024), HiVE-MIL (Wong et al. 2025), HDMIL (Wong et al. 2025), and FOCUS (Guo et al. 2025) aim to reduce inference-time computation by selectively analyzing task-relevant patches. While effective at filtering irrelevant regions, these approaches still require full high-resolution patch extraction and encoding, resulting in significant computational and memory overhead that limits scalability.

To address these limitations, we propose **WISE-FUSE**, a method that selects diagnostically relevant patches in a coarse-to-fine manner without the need to exhaustively encode all high-resolution patches or train a separate ROI selector. The key idea is to leverage recent vision-language models (VLMs) tailored to medical and pathology domains, which provide rich textual descriptions aligned with visual features in pathology images. By filtering low-resolution patches based on class-specific morphological descriptions using a pathology VLM in a zero-shot fashion, large portions of diagnostically irrelevant patches can be discarded early, allowing computational resources to focus on diagnostically meaningful regions. However, a critical challenge in this approach is that low-resolution images lack the fine-grained visual cues—such as cellular-level morphological features—that are essential for accurate diagnosis. To address this, we propose Cross-Scale Visual Prompt Tuning (CS-VPT), which distills high-resolution visual information into low-resolution representations, ensuring that subtle diagnostic features are preserved in low-resolution patch features. Additionally, we incorporate large language models (LLMs), such as GPT-4 (Achiam et al. 2023) and Gemini (Team et al. 2023), to compensate for potential information loss during patch selection and to enhance the representations with contextual and semantic knowledge. The main contributions are summarized as follows:

- We propose the novel approach in CPath that leverages VLMs for efficient patch selection and encoding for WSIs. The method is model-agnostic and can be seamlessly integrated with any CLIP-like VLM. We demonstrate the generalizability of our method across three different VLMs in the result section.
- We propose CS-VPT, which distills high-resolution information into low-resolution representations via learnable prompts trained on a few representative slides. This enables effective selection of salient patches at a coarse level while preserving fine-grained diagnostic features.
- We further introduce a cross-modal knowledge fusion mechanism that enriches selected patch embeddings with LLM-derived morphological cues. This compensates for potential information loss during patch selection and enhances diagnostic performance.
- Through extensive experiments across multiple datasets and downstream tasks, we demonstrate that WISE-FUSE reduces WSI encoding time by an order of magnitude, while achieving performance that is comparable to—or even surpass—those obtained by processing all patches (Figure 1).

We believe the proposed approach marks a significant step toward the practical deployment of VLMs and LLMs

in CPath, offering a scalable and efficient solution for analyzing complex WSIs while maintaining the completeness and richness of diagnostic information.

## Related Work

### 2.1 ROI Detection & Patch Selection in CPath

To address the high computational cost of processing gigapixel WSIs, numerous approaches have been proposed to identify diagnostically relevant regions. Early methods focus on Region-of-Interest (ROI) detection. Huang et al. (Huang and Li 2020) proposed a low-level feature and superpixel segmentation-based ROI selection algorithm, while Nugaliyadde et al. (Nugaliyadde et al. 2020) and Hossain et al. (Hossain et al. 2023) employed convolutional neural networks and vision transformers to automate ROI extraction. Korkut et al. (Korkut, Erkan, and Aksoy 2023) further showed that ROI-centric analysis can enhance classification performance. However, these methods mostly **rely on extensive annotations or pretrained ROI detectors**, which are costly and limit their scalability across tasks or datasets.

To mitigate the computational burden during inference, patch selection strategies have also been explored. SMT (Yu et al. 2024) mimics the diagnostic workflow of pathologists by progressively zooming in from low-resolution thumbnails to selectively analyze high-resolution regions. HiVE-MIL (Wong et al. 2025) utilizes a pathology-pretrained vision-language model to compute similarities between low-resolution patches and class-specific prompts, masking irrelevant regions and propagating relevance to high-resolution counterparts. HDMIL (Dong et al. 2025) adopts a differentiable binarization scheme using the Gumbel-sigmoid trick to select task-relevant patches while maintaining consistency with a full-resolution teacher. FOCUS (Guo et al. 2025) removes redundant patches via a sliding window mechanism and aggregates visually similar ones using language-guided token selection and pairwise similarity. While these patch selection methods reduce inference-time computation by filtering out irrelevant regions, they share a key limitation with ROI detection approaches: **during training, all high-resolution patches still need to be extracted and encoded**, leading to high computational and memory costs that undermine their overall scalability.

### 2.2 Vision-Language Models in CPath

Recent advancements in VLMs and foundation models have revolutionized performance in natural image and text tasks. CLIP (Radford et al. 2021) aligned image and language representations via contrastive learning, effectively bridging the gap between modalities. Building on this idea, Flamingo (Alayrac et al. 2022) introduced a perceiver resampler that leverages powerful language models to efficiently integrate visual information, achieving strong performance on diverse visual-language tasks even in few-shot scenarios. Similarly, CoCa (Yu et al. 2022) combined contrastive and captioning losses during pretraining to develop an image-text encoder-decoder model that generalizes well across a broad range of tasks. Inspired by these successes, researchers have begun to extend VLM techniques to the

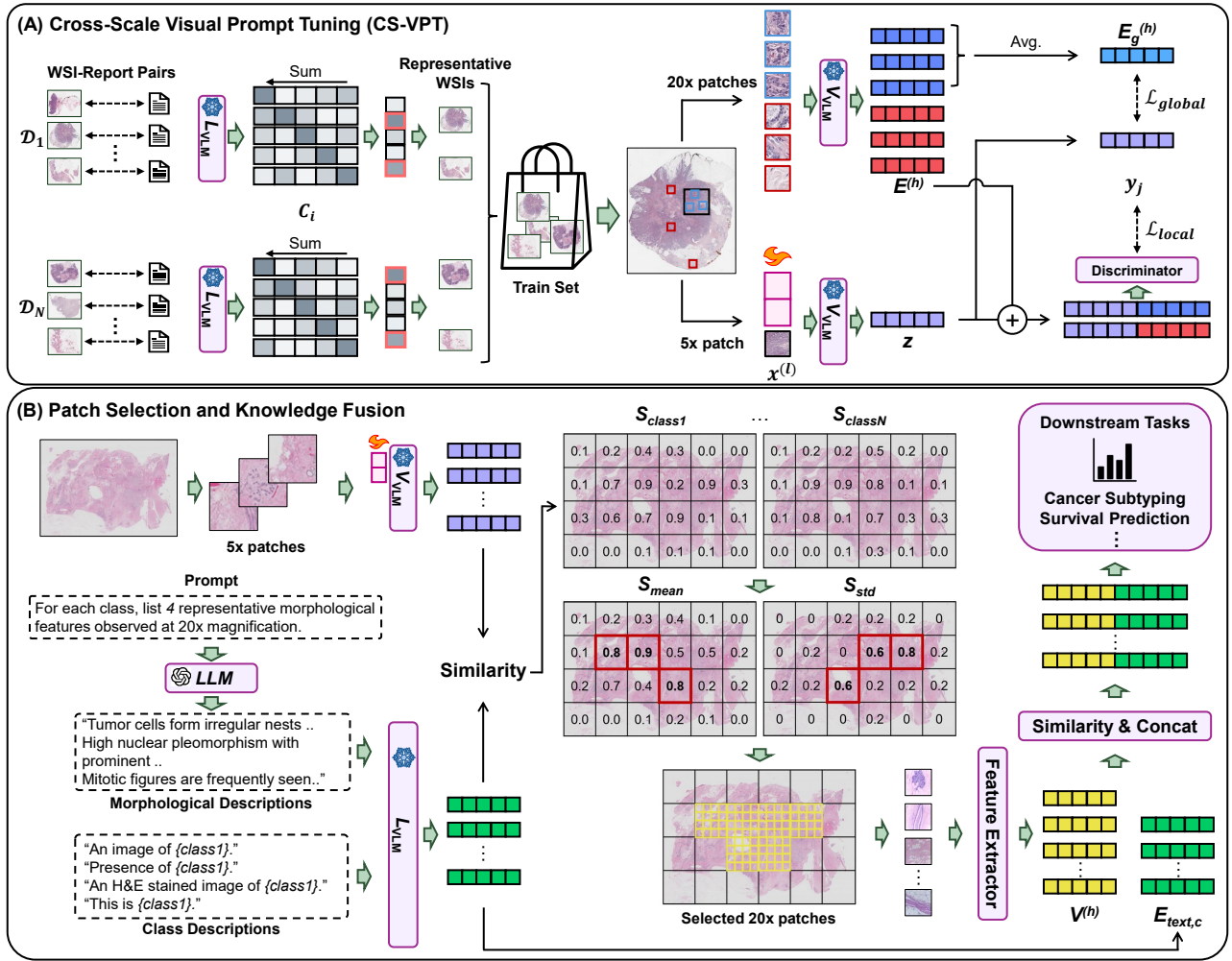


Figure 2: Overview of our **WISE-FUSE** framework. (A) cross-scale visual prompt tuning (CS-VPT) is performed by selecting  $n$  representative WSIs per class based on diagnostic reports, and distilling high-resolution patch information into corresponding low-resolution patches. (B) Diagnostic patch selection is conducted by computing the similarity between the features of low-resolution patches—enhanced via distillation—and class-specific textual descriptions. The selected patches are used for downstream tasks after undergoing cross-modal fusion with textual features.

medical domain. BiomedCLIP (Zhang et al. 2023) expanded CLIP’s framework by constructing the PMC-15M dataset, which contains 15 million image–text pairs extracted from 4.4 million scientific articles. In parallel, PLIP (Huang et al. 2023) curated pathology-specific image–text pairs from public forums such as Twitter to establish a specialized foundational model for pathology. CONCH (Lu et al. 2024) extended this line of work by enlarging the available datasets and broadening the scope of downstream tasks to include not only classification but also generative tasks like image captioning. QuiltNet (Oluchi Ikezogwo et al. 2023) continued this trajectory by constructing QUILT-1M from expert-narrated videos and achieving state-of-the-art performance across classification and retrieval tasks. Although prior studies underscore the powerful synergy of vision and language modalities in digital pathology, **none have yet proposed a principled framework for efficiently handling gigapixel**

**WSIs using VLMs.** This work represents an initial effort in that direction.

## Method

This work introduces WISE-FUSE that fully exploits the strengths of a pathology-specialized VLM and an LLM to selectively identify a diagnostically critical subset of patches in WSIs, as illustrated in Figure 2. We selectively identify the most diagnostically relevant areas in the WSI based on low-resolution representations by computing the similarity between text embeddings and visual embeddings from a pre-trained VLM. To mitigate the risk of omitting the fine-grained information by using low-resolution patches, we first select a few representative WSIs per task and perform VPT to distill the knowledge from high-resolution patches into low-resolution representations. Then, we conduct a top- $k$  selection based on the similarity between these

enhanced low-resolution embeddings and the text embeddings, and subsequently encode the corresponding high-resolution patches. Additionally, to recover any information lost during patch selection, we leverage an LLM to extract critical morphological details and incorporate them into the patch representations according to their importance.

### 3.1 Fine-to-Coarse Distillation via CS-VPT

**Selecting Representative WSIs** We first select representative WSIs for each target downstream task using pathology report information obtained from TCGA (Kefeli and Tatonetti 2024). Given a dataset  $\mathcal{D}_c$  corresponding to a specific class  $c$ , we extract textual reports associated with each sample and encode them using the VLM’s text encoder ( $L_{\text{VLM}}$ ). Let  $r_i \in \mathbb{R}^d$  denote the embedding of the  $i$ -th report. To identify the most representative samples for each class, we compute pairwise cosine similarities between embeddings and aggregate them as follows:

$$C_i = \text{Softmax} \left( \sum_{j \in \mathcal{D}_c} \frac{r_i \cdot r_j}{\|r_i\| \|r_j\|} \right) \quad (1)$$

for all  $i, j \in \mathcal{D}_c$ . The top  $n$  samples with the highest similarity scores  $C_i$  are selected as representative slides, where we set  $n = 5$  in our experiments.

Once the representative slides are selected, we generate high-resolution and low-resolution patches for further processing. We extract high-resolution patches at  $20\times$  magnification and low-resolution patches at  $5\times$ , reflecting fine-grained and coarse-level tissue features, respectively.

**VPT for Knowledge Distillation** To distill knowledge from high-resolution patches into their low-resolution counterparts, we perform visual prompt tuning, known as VPT. For each WSI, we extract high-resolution embeddings ( $E^{(h)}$ ) from  $20\times$  patches using the VLM’s vision encoder ( $V_{\text{VLM}}$ ) and obtain their corresponding low-resolution patches at  $5\times$  magnification ( $x^{(l)}$ ). The dataset consists of triplets  $(x^{(l)}, E_g^{(h)}, E^{(h)})$ , where the global embedding  $E_g^{(h)}$  is defined as the mean embedding of all high-resolution patches within the region of  $x^{(l)}$ :

$$E_g^{(h)} = \frac{1}{|\mathcal{R}(x^{(l)})|} \sum_{i \in \mathcal{R}(x^{(l)})} e_i^{(h)}. \quad (2)$$

Here,  $\mathcal{R}(x^{(l)})$  denotes the set of high-resolution patches within the spatial region of  $x^{(l)}$ , and  $e_i^{(h)}$  represents their respective embeddings. Positive patches are high-resolution patches within  $\mathcal{R}(x^{(l)})$ , while negative patches are randomly sampled from outside this region. Finally, learnable prompt embeddings  $P$  are integrated into  $V_{\text{VLM}}$ :

$$z = V_{\text{VLM}}(x^{(l)}, P), \quad (3)$$

where  $z$  is the output embedding of the low-resolution patch.

For distillation, we introduce two learning objectives: global alignment and local discrimination. The global alignment loss encourages the low-resolution embedding  $z$  to

capture the holistic information of the high-resolution region by minimizing the KL divergence between their distributions:

$$\mathcal{L}_{\text{global}} = D_{\text{KL}}(\text{softmax}(E_g^{(h)}) \parallel \text{softmax}(z)). \quad (4)$$

The local contrastive loss is to accelerate the fine-to-coarse knowledge distillation. We achieve this by employing a discriminator  $D$  that classifies whether a given high-resolution patch  $e_j^{(h)}$  belongs to the region of  $x^{(l)}$ . The loss is formulated as a binary cross-entropy (BCE) loss:

$$\mathcal{L}_{\text{local}} = \frac{1}{M} \sum_{j=1}^M \text{BCE}(D(z, e_j^{(h)}), y_j), \quad (5)$$

where  $y_j$  is a binary label indicating whether  $e_j^{(h)}$  is a positive ( $y_j = 1$ ) or negative ( $y_j = 0$ ) patch. To jointly optimize these objectives, we define the total loss function as:

$$\mathcal{L}_{\text{tot}} = \lambda_1 \mathcal{L}_{\text{global}} + \lambda_2 \mathcal{L}_{\text{local}}. \quad (6)$$

During training, only  $P$  and the projection layer of  $V_{\text{VLM}}$  are optimized and all of the model parameters are frozen.

### 3.2 Coarse-to-Fine Patch Selection and WSI Encoding using VLM and LLM

**Patch selection** To compute the similarity between textual descriptions and low-resolution patch embeddings, we first design text prompts. Since the CS-VPT module is trained to transfer fine-grained high-resolution knowledge to low-resolution patches, we incorporate morphological features that are typically observed in high-resolution patches for each class. The morphological characteristics observed at  $20\times$  magnification for each class are extracted using an LLM such as GPT-4o. These descriptions are then encoded using the VLM’s text encoder ( $L_{\text{VLM}}$ ), where we obtain both the class name embedding  $E_{\text{class},c}$  and the morphological feature embedding  $E_{\text{morph},c}$ . The final text embedding for each class is computed as:

$$E_{\text{text},c} = \frac{1}{2} (E_{\text{class},c} + E_{\text{morph},c}). \quad (7)$$

Given a set of  $5\times$  patches  $x_i^{(l)}$ , we extract their embeddings using the VLM’s vision encoder  $V_{\text{VLM}}$ :

$$E_i^{(l)} = V_{\text{VLM}}(x_i^{(l)}, P), \quad (8)$$

where  $E_i^{(l)}$  represents the embedding of patch  $x_i^{(l)}$ . We then compute the similarity score between each patch embedding and class-specific text embeddings using cosine similarity:

$$S_{i,c} = \frac{E_i^{(l)} \cdot E_{\text{text},c}}{\|E_i^{(l)}\| \|E_{\text{text},c}\|}. \quad (9)$$

To integrate class-wise similarity information effectively, we define two key selection principles:

1. Patches with consistently high similarity scores across multiple classes contain generally important diagnostic information.

2. Patches exhibiting large inter-class similarity score variance highlight class-discriminative regions essential for classification.

Based on these principles, we transform the original similarity matrix  $S_{i,c}$  into two statistical measures: the mean similarity score across all classes,  $S_i^{\text{mean}} = \text{mean}(S_{i,c})$ , and the standard deviation of similarity scores for each patch,  $S_i^{\text{std}} = \text{std}(S_{i,c})$ . For the final selection, we firstly select top  $k/2$  patches based on  $S_i^{\text{mean}}$ , ensuring that generally informative patches are retained. After that, from the remaining patches, the top  $k/2$  patches are selected based on  $S_i^{\text{std}}$ , prioritizing patches with strong class-discriminative properties. In our setting, we set  $k$  as 10% of the total number of  $5\times$  patches within the slide. The  $20\times$  patches corresponding to the selected  $5\times$  patches are then used for the downstream task, preserving both general and class-specific critical regions efficiently.

**Morphological knowledge fusion** The patch selection process inevitably leads to some degree of information loss. To mitigate this, we leverage the alignment capabilities of VLM and the powerful performance of existing LLM to compensate for missing information. This is achieved by integrating textual information into the selected patch representations. For each low-resolution patch  $x_i^{(l)}$ , we generate a weighted text representation based on the similarity scores  $S_{i,c}$ . Specifically, the final text vector  $E_{\text{text},i}$  for each patch is computed as a weighted sum of class-specific text embeddings:

$$E_{\text{text},i} = \sum_c S_{i,c} \cdot E_{\text{text},c}. \quad (10)$$

To do this, the contribution of textual knowledge is proportional to the relevance of the patch to each class. To integrate textual knowledge into the visual representation, we concatenate the 1D text vector  $E_{\text{text},i}$  with the corresponding visual feature  $V_i^{(h)}$  extracted from visual extractor:

$$V_i^{(h)} \leftarrow \text{Concat}(V_i^{(h)}, E_{\text{text},i}). \quad (11)$$

The enriched visual-textual feature  $V_i^{(h)}$  is then used for downstream tasks, ensuring that the information lost during the patch selection process is compensated for with the support of morphological knowledge fusion.

## Experiment

### 4.1 Experimental Setup

**Datasets** We evaluated our method using publicly available datasets from the Cancer Genome Atlas (TCGA) (Kefeli and Tatonetti 2024). Our experiments covered four cancer types: BRCA, NSCLC, RCC, and COAD, each associated with different downstream classification tasks. Specifically, for BRCA, the dataset includes Invasive Ductal Carcinoma (IDC) and Invasive Lobular Carcinoma (ILC) for cancer subtyping, surviving and deceased cases for survival prediction, and four molecular subtypes: Luminal A (LumA), Luminal B (LumB), Basal-like, and HER2-enriched for molecular profiling. For NSCLC, we considered Lung Adenocarcinoma (LUAD) and Lung Squamous Cell Carcinoma

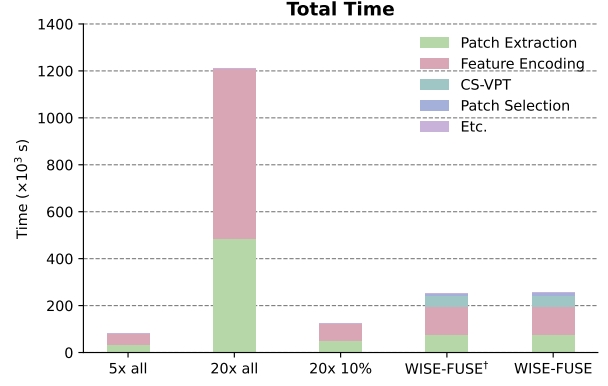


Figure 3: Bar plot of WSI processing time analysis on the TCGA-NSCLC dataset. ‘Etc.’ refers to text feature extraction and similarity score computation for knowledge fusion. Note that patch extraction and per-patch feature encoding are the major bottlenecks, and WISE-FUSE significantly reduces them with minimal overhead.

(LUSC) for subtyping, and surviving vs. deceased labels for survival analysis. The RCC dataset comprises three subtypes for classification: Clear Cell RCC (CCRCC), Papillary RCC (PRCC), and Chromophobe RCC (CHRC). Lastly, for COAD, we utilized surviving and deceased outcomes for survival prediction. For qualitative assessment, we employed the BACH dataset (Pol nia, Eloy, and Aguiar 2020), which consists of H&E-stained breast histology microscopy WSIs with pixel-level tumor region annotations.

**Metrics** We evaluated model performance using three standard metrics: accuracy, weighted F1-score, and area under the ROC curve (AUC). Accuracy measures overall classification correctness, while the weighted F1-score accounts for class imbalance by averaging per-class F1-scores weighted by support. AUC provides a threshold-independent assessment of the model’s discriminative ability.

**Implementation Details** The validation is performed across three pathology VLMs: CONCH, PLIP, and Biomed-CLIP. After completing the patch selection process, we utilized the visual encoder of CONCH as a feature extractor. Each task was subsequently evaluated using IBMIL (Lin et al. 2023) with a 5-fold cross-validation setup. Except for VPT, all hyperparameters, including those for IBMIL, followed the settings of the original studies. For VPT, we used 30 learnable prompts and optimized the model with the Adam optimizer at a learning rate of  $1e-4$ .

### 4.2 Quantitative Results

**Classification Performance** Table 1 and 2 present the results on cancer subtyping and survival prediction, which are commonly addressed downstream tasks in digital pathology. “ $5\times$  all” uses all low resolution patches, “ $20\times$  all” uses all high resolution patches, and “ $20\times$  10%” uses 10% of randomly sampled  $20\times$  patches. We denote WISE-FUSE† as the variant that applies patch selection only, without in-

Model	Method	TCGA-BRCA			TCGA-NSCLC			TCGA-RCC		
		ACC	W_F1	AUC	ACC	W_F1	AUC	ACC	W_F1	AUC
–	5× all	82.1	84.3	89.2	91.8	92.4	97.6	89.8	91.8	98.8
	20× all	85.4	86.3	90.3	92.2	92.8	97.3	88.6	91.2	98.1
	20× 10%	83.1	84.3	88.2	89.3	90.9	95.8	86.6	90.1	96.3
CONCH	WISE-FUSE <sup>†</sup>	86.2	87.2	90.3	<b>91.9</b>	<b>92.4</b>	95.9	88.3	<b>91.1</b>	97.3
	WISE-FUSE	<b>89.3</b>	<b>89.3</b>	<b>90.6</b>	<b>91.9</b>	<b>92.4</b>	<b>96.0</b>	<b>88.8</b>	90.8	<b>97.6</b>
PLIP	WISE-FUSE <sup>†</sup>	83.8	84.6	88.7	<b>90.5</b>	<b>90.8</b>	<b>95.5</b>	86.8	90.4	<b>98.2</b>
	WISE-FUSE	<b>86.9</b>	<b>87.6</b>	<b>92.8</b>	90.4	90.7	95.4	<b>87.8</b>	<b>90.6</b>	98.0
Biomed CLIP	WISE-FUSE <sup>†</sup>	87.3	87.4	90.5	89.6	90.0	<b>96.4</b>	<b>88.5</b>	<b>91.0</b>	<b>98.3</b>
	WISE-FUSE	<b>88.2</b>	<b>88.9</b>	<b>93.0</b>	<b>90.5</b>	<b>90.9</b>	96.1	88.3	90.7	98.0

Table 1: Performance of cancer subtyping using MIL on TCGA-BRCA, TCGA-NSCLC, and TCGA-RCC. <sup>†</sup> denotes the variant without knowledge fusion (patch selection only).

Model	Method	TCGA-BRCA			TCGA-NSCLC			TCGA-COAD		
		ACC	W_F1	AUC	ACC	W_F1	AUC	ACC	W_F1	AUC
–	5× all	60.5	62.5	54.7	55.3	56.2	61.3	64.3	68.9	64.1
	20× all	62.2	67.8	58.5	57.6	56.5	62.4	66.1	68.6	66.5
	20× 10%	56.0	64.3	57.1	53.4	54.1	60.9	65.0	67.7	66.8
CONCH	WISE-FUSE <sup>†</sup>	65.4	69.2	60.4	58.7	<b>59.3</b>	<b>63.3</b>	70.2	73.3	66.6
	WISE-FUSE	<b>66.2</b>	<b>69.9</b>	<b>61.3</b>	<b>59.3</b>	58.7	60.9	<b>72.0</b>	<b>73.9</b>	<b>73.2</b>
PLIP	WISE-FUSE <sup>†</sup>	<b>62.1</b>	<b>67.0</b>	<b>60.0</b>	<b>58.3</b>	<b>57.8</b>	<b>61.9</b>	65.0	69.0	<b>66.5</b>
	WISE-FUSE	57.5	63.2	59.5	57.1	54.1	59.5	<b>67.9</b>	<b>70.1</b>	65.7
Biomed CLIP	WISE-FUSE <sup>†</sup>	64.3	<b>69.0</b>	58.8	56.0	55.4	<b>63.4</b>	<b>67.8</b>	<b>71.5</b>	<b>64.5</b>
	WISE-FUSE	<b>64.5</b>	<b>69.0</b>	<b>60.8</b>	<b>58.5</b>	<b>58.2</b>	63.0	64.0	68.9	63.7

Table 2: Performance of survival prediction using MIL on TCGA-BRCA, TCGA-NSCLC, and TCGA-COAD. <sup>†</sup> denotes the variant without knowledge fusion (patch selection only).

corporating knowledge fusion for enhancing patch embeddings. In most settings, our method consistently outperforms random patch selection at the same patch ratio (i.e., the number of patches used), demonstrating its ability to effectively identify diagnostically relevant regions. Remarkably, despite using only one-tenth of the patches, our method achieves comparable or even superior classification performance to the full-resolution baseline that processes all high-resolution patches (“20× all” vs. WISE-FUSE). This performance gap is particularly evident in survival prediction tasks, where even without knowledge fusion, the selection of a small set of highly informative patches yields better results than exhaustive patch usage. These findings highlight the robustness and generalizability of WISE-FUSE, which combines selective patch processing with cross-modal knowledge fusion. The method performs consistently well across datasets, task types, and vision-language backbones, underscoring its task and model agnostic effectiveness in computational pathology. Additional results on molecular profiling and metastasis prediction are in Supplementary Section 3.1.

**Runtime Analysis** Figure 3 illustrates the total processing time required by each method on the TCGA-NSCLC dataset with an NVIDIA RTX 4090 GPU. Although preprocessing all high-resolution patches requires approximately two weeks in our setting, WISE-FUSE reduces the patch

ratio to 10%, bringing the total processing time down to less than three days, a more than fourfold improvement. As the size of dataset increases, this efficiency gain becomes even more critical. Although our framework introduces additional steps such as low-resolution patch preprocessing, cross-scale knowledge distillation via CS-VPT, and similarity matrix computation between patch and text embeddings, these components incur substantially less overhead compared to high-resolution patch processing. Consequently, WISE-FUSE maintains a clear advantage in terms of time cost.

### 4.3 Qualitative Results

To further validate the effectiveness of WISE-FUSE, we conducted a qualitative analysis. Figure 4 illustrates how CS-VPT improves the quality of patch selection. Since the TCGA datasets lack pixel-level region-of-interest (ROI) annotations, we fine-tuned the CONCH model on TCGA-BRCA and evaluated it on the BACH dataset, which provides pixel-level annotations. After applying CS-VPT, the number of selected invasive patches increased from 63 to 74, while the frequency of background or normal tissue being selected was significantly reduced compared to the setting without CS-VPT. Nonetheless, some normal tissue patches were still selected, which we attribute to the zero-shot evaluation setting on the BACH dataset.

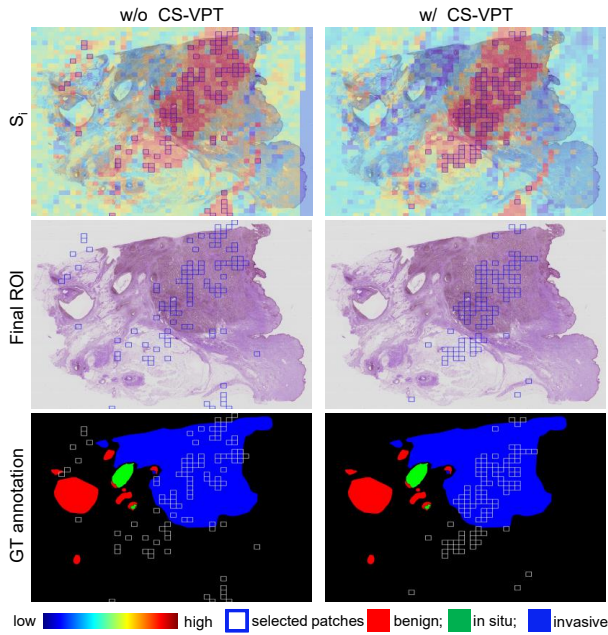


Figure 4: Visualization of selected patches based on the similarity score between coarse patches and text embeddings for different samples.  $S_i$  means similarity score-based heatmap.

Figure 5 compares our selected patches with the attention heatmaps generated by ABMIL trained on all patches. Across four different WSIs, we observed that our method consistently selects regions with high attention scores, indicating strong diagnostic relevance. This demonstrates that WISE-FUSE can effectively identify critical regions without processing the entire slide, achieving significant reductions in processing time while maintaining diagnostic fidelity.

CS-VPT	Morpho descriptions	Knowledge Fusion	ACC	W_F1	AUC
✗	✗	✗	83.8	85.0	88.4
✓	✗	✗	85.5	86.3	90.1
✓	✓	✗	86.3	87.2	90.3
✓	✓	✓	<b>89.3</b>	<b>89.3</b>	<b>90.6</b>

Table 3: Ablation study of each component in WISE-FUSE on TCGA-BRCA cancer subtyping. The vision-language backbone used in this experiment is CONCH.

#### 4.4 Ablation Study

Table 3 summarizes the results of the ablation study, illustrating each component’s contribution. The ‘Morpho descriptions’ refer to the incorporation of LLM-derived morphological knowledge into the class descriptions used for patch selection. We observed a gradual improvement in classification performance as each component is added. CS-VPT enables the VLM to consider fine-grained details by distilling high-resolution patch embeddings into their low-

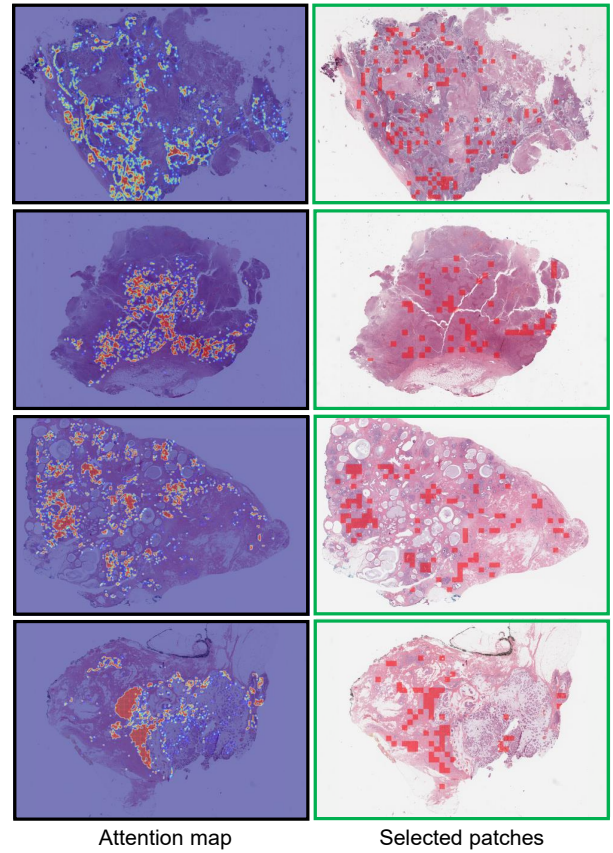


Figure 5: Visual comparison of ABMIL attention heatmap (black) and patch selection results from WISE-FUSE (green) on representative WSIs. Note that WISE-FUSE can select diagnostically relevant patches without processing the entire region as ABMIL.

resolution counterparts, thereby facilitating more accurate identification of diagnostically relevant patches. Additionally, the morphological expressions extracted from the LLM further enhance the patch selection process by guiding the model to focus on clinically important regions. In particular, knowledge fusion leads to a substantial performance gain, demonstrating the effectiveness of cross-modal integration in compensating for missing or limited information.

## Conclusion

In this paper, we introduce WISE-FUSE for efficiently encoding large-scale WSIs, addressing a critical need in clinical computational pathology. Leveraging the capabilities of pre-trained VLMs and LLMs, WISE-FUSE adopts a coarse-to-fine patch selection strategy that identifies diagnostically relevant regions without the need to process all patches. WISE-FUSE reduces processing time by over threefold on average across datasets, while achieving superior diagnostic performance compared to full-resolution baselines by processing only a small subset of informative patches. Quantitative evaluations across multiple tasks highlight the effectiveness and scalability of WISE-FUSE. Nevertheless, sev-

eral components in the framework rely on the quality of pre-trained VLMs and LLMs, which is an interesting future research direction to improve.

## References

- Achiam, J.; Adler, S.; Agarwal, S.; Ahmad, L.; Akkaya, I.; Aleman, F. L.; Almeida, D.; Altenschmidt, J.; Altman, S.; Anadkat, S.; et al. 2023. GPT-4 technical report. *arXiv preprint arXiv:2303.08774*.
- Alayrac, J.-B.; Donahue, J.; Luc, P.; Miech, A.; Barr, I.; Hasson, Y.; Lenc, K.; Mensch, A.; Millican, K.; Reynolds, M.; et al. 2022. Flamingo: a visual language model for few-shot learning. *Advances in neural information processing systems*, 35: 23716–23736.
- Dong, J.; Jiang, J.; Jiang, K.; Li, J.; and Zhang, Y. 2025. Fast and Accurate Gigapixel Pathological Image Classification with Hierarchical Distillation Multi-Instance Learning. In *Proceedings of the Computer Vision and Pattern Recognition Conference*, 30818–30828.
- Guo, Z.; Xiong, C.; Ma, J.; Sun, Q.; Feng, L.; Wang, J.; and Chen, H. 2025. Focus: Knowledge-enhanced adaptive visual compression for few-shot whole slide image classification. In *Proceedings of the Computer Vision and Pattern Recognition Conference*, 15590–15600.
- Hossain, M. S.; Shahriar, G. M.; Syeed, M. M.; Uddin, M. F.; Hasan, M.; Shivam, S.; and Advani, S. 2023. Region of interest (ROI) selection using vision transformer for automatic analysis using whole slide images. *Scientific Reports*, 13(1): 11314.
- Huang, J.; and Li, R. 2020. Fast regions-of-interest detection in whole slide histopathology images. In *Pathology-From Classics to Innovations*. IntechOpen.
- Huang, Z.; Bianchi, F.; Yuksekgonul, M.; Montine, T. J.; and Zou, J. 2023. A visual-language foundation model for pathology image analysis using medical twitter. *Nature medicine*, 29(9): 2307–2316.
- Ilse, M.; Tomczak, J.; and Welling, M. 2018. Attention-based Deep Multiple Instance Learning. In Dy, J.; and Krause, A., eds., *Proceedings of the 35th International Conference on Machine Learning*, volume 80 of *Proceedings of Machine Learning Research*, 2127–2136. PMLR.
- Kefeli, J.; and Tatonetti, N. 2024. TCGA-Reports: A machine-readable pathology report resource for benchmarking text-based AI models. *Patterns*, 5(3).
- Korkut, S.; Erkan, C.; and Aksoy, S. 2023. On the benefits of region of interest detection for whole slide image classification. In *Medical Imaging 2023: Digital and Computational Pathology*, volume 12471, 155–163. SPIE.
- Lin, T.; Yu, Z.; Hu, H.; Xu, Y.; and Chen, C.-W. 2023. Interventional bag multi-instance learning on whole-slide pathological images. In *Proceedings of the IEEE/CVF Conference on Computer Vision and Pattern Recognition*, 19830–19839.
- Lu, M. Y.; Chen, B.; Williamson, D. F.; Chen, R. J.; Liang, I.; Ding, T.; Jaume, G.; Odintsov, I.; Le, L. P.; Gerber, G.; et al. 2024. A visual-language foundation model for computational pathology. *Nature Medicine*, 30(3): 863–874.
- Nugaliyadde, A.; Wong, K. W.; Parry, J.; Sohel, F.; Laga, H.; Somaratne, U. V.; Yeomans, C.; and Foster, O. 2020. RCNN for region of interest detection in whole slide images. In *Neural Information Processing: 27th International Conference, ICONIP 2020, Bangkok, Thailand, November 18–22, 2020, Proceedings, Part V* 27, 625–632. Springer.
- Oluchi Ikezogwo, W.; Saygin Seyfioglu, M.; Ghezloo, F.; Geva, D. S. C.; Mohammed, F. S.; Anand, P. K.; Krishna, R.; and Shapiro, L. 2023. Quilt-1M: One Million Image-Text Pairs for Histopathology. *arXiv e-prints*, arXiv–2306.
- Polónia, A.; Eloy, C.; and Aguiar, P. 2020. BACH Dataset : Grand Challenge on Breast Cancer Histology images.
- Radford, A.; Kim, J. W.; Hallacy, C.; Ramesh, A.; Goh, G.; Agarwal, S.; Sastry, G.; Askell, A.; Mishkin, P.; Clark, J.; et al. 2021. Learning transferable visual models from natural language supervision. In *International conference on machine learning*, 8748–8763. PMLR.
- Team, G.; Anil, R.; Borgeaud, S.; Alayrac, J.-B.; Yu, J.; Soricut, R.; Schalkwyk, J.; Dai, A. M.; Hauth, A.; Millican, K.; et al. 2023. Gemini: a family of highly capable multimodal models. *arXiv preprint arXiv:2312.11805*.
- Wong, B.; Kim, J. W.; Fu, H.; and Yi, M. Y. 2025. Few-Shot Learning from Gigapixel Images via Hierarchical Vision-Language Alignment and Modeling. *arXiv preprint arXiv:2505.17982*.
- Yu, J.; Wang, Z.; Vasudevan, V.; Yeung, L.; Seyedhosseini, M.; and Wu, Y. 2022. Coca: Contrastive captioners are image-text foundation models. *arXiv preprint arXiv:2205.01917*.
- Yu, X.; Luo, H.; Hu, J.; Zhang, X.; Wang, Y.; Liang, W.; Bei, Y.; Song, M.; and Feng, Z. 2024. Hundredfold accelerating for pathological images diagnosis and prognosis through self-reform critical region focusing. In *33rd Int. Joint Conf. on Artificial Intelligence*, 1607–1615.
- Zhang, S.; Xu, Y.; Usuyama, N.; Xu, H.; Bagga, J.; Tinn, R.; Preston, S.; Rao, R.; Wei, M.; Valluri, N.; et al. 2023. BiomedCLIP: a multimodal biomedical foundation model pretrained from fifteen million scientific image-text pairs. *arXiv preprint arXiv:2303.00915*.

# WISE-FUSE: Efficient Whole Slide Image Encoding via Coarse-to-Fine Patch Selection with VLM and LLM Knowledge Fusion

## Supplementary Material

### 1. Dataset Statistics

For our experiments, we used five publicly available datasets from The Cancer Genome Atlas (TCGA): BRCA, NSCLC, RCC, COAD, and STAD (results on STAD are included in the supplementary only). All WSIs were preprocessed by removing background regions using Otsu’s thresholding, and image patches were extracted with a fixed size of 256×256 pixels. We utilized 5× magnification for low-resolution patches and 20× magnification for high-resolution patches. Table 4 summarizes the number of slides and extracted patches at low and high magnifications.

Dataset	# Slides	# 5× patches	# 20× patches
TCGA-BRCA	1,003	539,327	7,716,660
TCGA-NSCLC	3,129	732,882	11,701,195
TCGA-RCC	3,066	1,019,700	16,354,162
TCGA-COAD	1,471	301,509	4,806,083
TCGA-STAD	484	236,836	3,818,986

Table 4: Number of slides and patches for each dataset.

### 2. Morphological Descriptions for Each Task

We provide class-specific morphological descriptions used for prompt construction in four major tasks: cancer subtyping, survival prediction, molecular profiling, and metastasis prediction. Each class is described with four representative observations typically seen at 20× magnification, covering architectural and cytological characteristics.

These descriptions were generated using GPT-4o by prompting the model with structured queries that specified the organ type, classification task, and class labels, similar to the prompting strategies employed in prior works (Wong et al. 2025). A representative prompt format is as follows:

```
The task is to summarize the morphological features of the {dataset} for the classes {class_1}, {class_2}, ..., {class_N}. For each class, list 4 representative morphological features observed at 20× magnification. Each feature should be in the form of a short sentence.
```

For example, the query used for cancer subtyping in TCGA-BRCA was:

```
The task is to summarize the morphological features of the BRCA for the classes invasive ductal carcinoma and invasive
```

```
lobular carcinoma. For each class, list 4 representative morphological features observed at 20× magnification. Each feature should be in the form of a short sentence.
```

Detailed morphological prompts for each task can be found in the following tables:

- **Table 5:** Cancer Subtyping
- **Table 6:** Survival Prediction
- **Table 7:** Molecular Profiling
- **Table 8:** Metastasis Prediction

### 3. Further Experimental Results

#### 3.1 Additional Tasks under the Same Framework

To further assess the generalizability of WISE-FUSE across diverse pathological tasks, we conducted experiments on additional classification problems, including molecular profiling and metastasis prediction, which were not included in the main paper. All experiments follow the same architecture, vision-language backbones (Lu et al. 2024), (Huang et al. 2023), (Zhang et al. 2023), training protocol, and patch resolution settings (5× for low-resolution and 20× for high-resolution) as in the main experiments. Results are summarized in Table 9.

Our method achieves consistently strong performance across these additional tasks, demonstrating its adaptability to a wide range of classification objectives in computational pathology. This suggests that our coarse-to-fine patch selection and knowledge fusion strategy are broadly applicable to various clinical endpoints.

#### 3.2 Effect of Using 1.25× as the Coarse Scale

To examine the trade-off between computational cost and diagnostic accuracy, we performed an ablation study in which the coarse-scale resolution was reduced from 5× to 1.25×. All other components of the pipeline were kept identical. Table 10, 11 and 12 report the classification performance under this setting.

Compared to the results using 5× patches (Table 1 and 2 in the main paper, Table 9 in the supplementary material), the overall classification performance tends to degrade when using 1.25× as the coarse scale. In particular, knowledge fusion that incorporates morphological descriptions often leads to diminished performance. This is likely due to the limited capability of the VLM to interpret extremely low-resolution pathological images such as those at 1.25×. Nevertheless, our method still achieves comparable or even superior performance to using all high-resolution patches,

supporting the validity of our mechanism that distills high-resolution information into low-resolution patches for selecting informative patches.

#### 4. Implementation Details

**Cross-Scale Visual Prompt Tuning (CS-VPT)** We provide training details of CS-VPT used for preserving fine-grained diagnostic features at a coarse level:

- **Number of training WSIs:** 5 slides per class
- **Number of learnable prompt:** 30
- **Number of epochs:** 200
- **Loss weights:**  $\lambda_1 = 500.0$ ,  $\lambda_2 = 1.0$
- **Learning rate:**  $1e-4$
- **Optimizer:** Adam
- **Batch size:** 64

**ABMIL Training** For MIL-based tasks, we follow the same data split protocol and training procedure across all datasets and tasks:

- **Data split:** 5-fold cross-validation with stratified split (8:1:1 train/val/test)
- **Number of epochs:** 100
- **Learning rate:**  $1e-4$
- **Loss function:** Binary cross-entropy loss with logits, implemented using `nn.BCEWithLogitsLoss()` for multi-label classification
- **Optimizer:** Adam
- **Early stopping:** Applied with patience of 20 epochs based on validation loss
- **Weight decay:**  $1e-4$
- **Learning rate scheduler:** CosineAnnealingLR

**System Configuration** All experiments were conducted on a machine with the following specifications:

- **GPU:** an NVIDIA RTX 4090
- **CPU:** Intel Xeon(R) Gold 6326 (64 cores)
- **RAM:** 1TB
- **PyTorch version:** 1.11.0
- **CUDA version:** 10.1

Dataset	Class	Morphological Descriptions (20×)
TCGA-BRCA	Invasive Ductal Carcinoma (IDC)	<ul style="list-style-type: none"> <li>• Tumor cells form irregular nests and cords infiltrating the stroma.</li> <li>• Desmoplastic stromal reaction is frequently observed surrounding tumor clusters.</li> <li>• High nuclear pleomorphism with prominent nucleoli is common.</li> <li>• Mitotic figures are frequently seen within the tumor cell population.</li> </ul>
	Invasive Lobular Carcinoma (ILC)	<ul style="list-style-type: none"> <li>• Tumor cells exhibit a single-file infiltration pattern through fibrous stroma.</li> <li>• Cells are small, uniform, and often lack significant nuclear pleomorphism.</li> <li>• Intracytoplasmic lumina or targetoid features may be present.</li> <li>• Tumor architecture often lacks cohesive glandular formation.</li> </ul>
TCGA-LSCLC	Lung Adenocarcinoma (LUAD)	<ul style="list-style-type: none"> <li>• Tumor displays acinar, papillary, or lepidic glandular growth patterns.</li> <li>• Cells have round to oval nuclei with moderate pleomorphism and visible nucleoli.</li> <li>• Mucin production is frequently observed within glandular lumina.</li> <li>• Stromal invasion is present with occasional desmoplastic reaction.</li> </ul>
	Lung Squamous Cell Carcinoma (LUSC)	<ul style="list-style-type: none"> <li>• Tumor forms solid nests or sheets with keratinization and intercellular bridges.</li> <li>• Cells exhibit abundant eosinophilic cytoplasm and irregular hyperchromatic nuclei.</li> <li>• Keratin pearls and individual cell keratinization are frequently seen.</li> <li>• Stromal regions often contain necrosis and dense inflammatory infiltration.</li> </ul>
TCGA-RCC	Clear Cell RCC (CCRCC)	<ul style="list-style-type: none"> <li>• Tumor cells have pale to eosinophilic cytoplasm with prominent cell borders.</li> <li>• Perinuclear clearing and wrinkled nuclei are commonly observed.</li> <li>• Architecture is composed of solid sheets or alveolar nests of cells.</li> <li>• Stromal regions are typically hyalinized with minimal inflammation.</li> </ul>
	Chromophobe RCC (CHRC)	<ul style="list-style-type: none"> <li>• Tumor cells display abundant clear cytoplasm with distinct cell membranes.</li> <li>• Nuclei show variable atypia and prominent nucleoli in high-grade areas.</li> <li>• Tumor forms nested or alveolar patterns separated by delicate vasculature.</li> <li>• Areas of hemorrhage and necrosis are frequently seen within tumor regions.</li> </ul>
	Papillary RCC (PRCC)	<ul style="list-style-type: none"> <li>• Tumor is composed of papillary or tubular structures lined by cuboidal to columnar cells.</li> <li>• Cells exhibit eosinophilic to basophilic cytoplasm with small, round nuclei.</li> <li>• Foamy macrophages and psammoma bodies are commonly present within papillary cores.</li> <li>• Fibrovascular stalks are frequently observed supporting papillary fronds.</li> </ul>

Table 5: Class-specific morphological prompts used for cancer subtyping.

Dataset	Class	Morphological Descriptions (20×)
TCGA-BRCA	Alive	<ul style="list-style-type: none"> <li>• Tumor cells exhibit low nuclear pleomorphism with small, uniform nuclei.</li> <li>• Glandular or tubular structures are well-formed and organized.</li> <li>• Mitotic activity is low with few visible mitotic figures.</li> <li>• The tumor-stroma interface is well-demarcated with limited invasion.</li> </ul>
	Dead	<ul style="list-style-type: none"> <li>• Tumor architecture is disorganized with sheets or solid nests of malignant cells.</li> <li>• Marked nuclear pleomorphism with hyperchromatic and irregular nuclei is present.</li> <li>• High mitotic rate with frequent atypical mitoses is observed.</li> <li>• Extensive stromal desmoplasia and lymphovascular invasion are frequently seen.</li> </ul>
TCGA-LSCLC	Alive	<ul style="list-style-type: none"> <li>• Tumor shows well-differentiated glandular or squamous architecture with preserved organization.</li> <li>• Nuclear pleomorphism is mild with infrequent mitotic figures.</li> <li>• Stromal invasion is limited with minimal necrosis or inflammation.</li> <li>• Lymphovascular and perineural invasion are rarely observed.</li> </ul>
	Dead	<ul style="list-style-type: none"> <li>• Tumor displays poorly differentiated or undifferentiated growth with architectural disarray.</li> <li>• Cells exhibit marked nuclear atypia and high mitotic activity with abnormal figures.</li> <li>• Extensive stromal desmoplasia, necrosis, and inflammatory infiltration are present.</li> <li>• Lymphovascular and perineural invasion are frequently seen at invasive fronts.</li> </ul>
TCGA-COAD	Alive	<ul style="list-style-type: none"> <li>• Tumor glands are well-formed with relatively preserved differentiation.</li> <li>• Nuclear pleomorphism is mild, and mitotic figures are sparse.</li> <li>• The tumor-stroma boundary is well-defined with limited invasion.</li> <li>• Lymphovascular and perineural invasion are rarely seen.</li> </ul>
	Dead	<ul style="list-style-type: none"> <li>• Tumor architecture is poorly differentiated with solid or cribriform growth patterns.</li> <li>• Marked nuclear atypia and frequent abnormal mitoses are observed.</li> <li>• Extensive lymphovascular and perineural invasion are commonly present.</li> <li>• Stromal desmoplasia and intratumoral necrosis are frequently seen.</li> </ul>

Table 6: Class-specific morphological prompts used for survival prediction.

Dataset	Class	Morphological Descriptions (20×)
TCGA-BRCA	Luminal A	<ul style="list-style-type: none"> <li>• Tumor cells show mild nuclear atypia with low mitotic activity.</li> <li>• Glandular structures are well-formed and retain luminal organization.</li> <li>• Stroma is relatively loose with minimal desmoplastic response.</li> <li>• Apical snouts and luminal secretions are often visible.</li> </ul>
	Luminal B	<ul style="list-style-type: none"> <li>• Tumor cells exhibit moderate nuclear pleomorphism and increased mitoses.</li> <li>• Glandular differentiation is present but less organized than in LumA.</li> <li>• Focal necrosis may be observed within tumor nests.</li> <li>• Stromal invasion is more pronounced with scattered lymphocytic infiltration.</li> </ul>
	Basal-like	<ul style="list-style-type: none"> <li>• Tumor cells form solid sheets with pushing borders and lack glandular structures.</li> <li>• High-grade nuclei with prominent nucleoli and brisk mitotic activity are common.</li> <li>• Central necrosis and comedo-like features are frequently seen.</li> <li>• Dense lymphocytic infiltrates are often present at the tumor periphery.</li> </ul>
	HER2-enriched	<ul style="list-style-type: none"> <li>• Tumor architecture is variable, ranging from solid to micropapillary patterns.</li> <li>• Cells show marked nuclear atypia and high mitotic index.</li> <li>• Areas of necrosis and calcification are commonly observed.</li> <li>• Stromal desmoplasia is prominent with frequent vascular invasion.</li> </ul>

Table 7: Class-specific morphological prompts used for molecular profiling in TCGA-BRCA.

Dataset	Class	Morphological Descriptions (20×)
TCGA-COAD	Node-negative (N0)	<ul style="list-style-type: none"> <li>• Tumor glands are moderately to well-differentiated with preserved architecture.</li> <li>• Nuclear atypia is mild, and mitotic figures are infrequent.</li> <li>• Tumor-stroma interface is smooth with limited infiltrative behavior.</li> <li>• Lymphovascular and perineural invasion are absent or rarely detected.</li> </ul>
	Node-positive (N+)	<ul style="list-style-type: none"> <li>• Glandular structures are irregular or lost, often replaced by solid or cribriform patterns.</li> <li>• Tumor cells show marked nuclear pleomorphism and high mitotic activity.</li> <li>• Lymphovascular invasion is frequently observed in peritumoral regions.</li> <li>• Desmoplastic stromal reaction and necrotic foci are commonly present.</li> </ul>
TCGA-STAD	Node-negative (N0)	<ul style="list-style-type: none"> <li>• Tumor shows well to moderately differentiated glandular structures with preserved polarity.</li> <li>• Nuclear pleomorphism is mild and mitotic figures are infrequent.</li> <li>• Tumor-stroma interface is smooth with limited invasive behavior.</li> <li>• Lymphovascular and perineural invasion are rarely identified.</li> </ul>
	Node-positive (N+)	<ul style="list-style-type: none"> <li>• Tumor displays poorly differentiated or diffuse growth with loss of glandular architecture.</li> <li>• Cells exhibit marked nuclear atypia and frequent abnormal mitotic figures.</li> <li>• Lymphovascular and perineural invasion are commonly observed in invasive fronts.</li> <li>• Desmoplastic stroma and intratumoral necrosis are frequently present.</li> </ul>

Table 8: Class-specific morphological prompts used for metastasis prediction in TCGA-COAD and TCGA-STAD.

Model	Method	TCGA-BRCA (Molecular profiling)			TCGA-COAD (Metastasis prediction)			TCGA-STAD (Metastasis prediction)		
		ACC	W_F1	AUC	ACC	W_F1	AUC	ACC	W_F1	AUC
–	5× all	28.0	57.7	72.8	52.3	54.6	59.5	56.7	55.4	59.8
	20× all	32.1	60.2	76.1	52.5	54.7	58.5	58.1	57.5	69.2
	20× 10%	31.8	60.0	75.7	51.5	53.1	57.9	57.5	55.9	60.7
CONCH	WISE-FUSE <sup>†</sup>	31.0	59.5	75.2	56.8	56.5	<b>62.5</b>	<b>61.5</b>	<b>62.5</b>	<b>69.5</b>
	WISE-FUSE	<b>41.5</b>	<b>61.2</b>	<b>77.8</b>	<b>58.5</b>	<b>58.9</b>	61.7	59.5	60.5	68.2
PLIP	WISE-FUSE <sup>†</sup>	30.4	62.5	75.0	53.7	53.5	61.9	<b>66.3</b>	<b>65.6</b>	<b>68.3</b>
	WISE-FUSE	<b>31.1</b>	<b>62.8</b>	<b>75.7</b>	<b>60.7</b>	<b>60.8</b>	<b>63.9</b>	54.4	54.5	65.9
Biomed CLIP	WISE-FUSE <sup>†</sup>	34.0	61.0	76.4	56.5	57.9	<b>61.5</b>	<b>60.2</b>	<b>61.4</b>	<b>64.4</b>
	WISE-FUSE	<b>45.3</b>	<b>63.1</b>	<b>79.8</b>	<b>57.4</b>	<b>58.6</b>	<b>61.5</b>	59.8	57.9	64.1

Table 9: Performance of molecular profiling and metastasis prediction using MIL on TCGA-BRCA, TCGA-COAD, and TCGA-STAD. <sup>†</sup> denotes the variant without knowledge fusion (patch selection only).

Model	Method	TCGA-BRCA			TCGA-NSCLC			TCGA-RCC		
		ACC	W_F1	AUC	ACC	W_F1	AUC	ACC	W_F1	AUC
–	1.25× all	82.0	83.7	87.3	84.2	84.9	93.6	81.5	87.5	96.8
	20× all	85.4	86.3	90.3	92.2	92.8	97.3	88.6	91.2	98.1
	20× 10%	83.1	84.3	88.2	89.3	90.9	95.8	86.6	90.1	96.3
CONCH	WISE-FUSE <sup>†</sup>	84.7	85.4	90.0	<b>90.0</b>	<b>90.2</b>	<b>96.8</b>	85.2	<b>88.5</b>	<b>97.7</b>
	WISE-FUSE	<b>88.5</b>	<b>89.2</b>	<b>90.7</b>	89.7	89.9	95.5	<b>85.6</b>	88.1	95.6
PLIP	WISE-FUSE <sup>†</sup>	79.4	81.0	85.7	89.5	90.5	95.8	87.2	<b>89.4</b>	<b>97.5</b>
	WISE-FUSE	<b>84.6</b>	<b>85.4</b>	<b>88.2</b>	<b>90.3</b>	<b>90.7</b>	<b>96.0</b>	<b>87.5</b>	89.2	97.4
Biomed CLIP	WISE-FUSE <sup>†</sup>	<b>87.8</b>	85.2	84.8	<b>89.1</b>	<b>89.6</b>	<b>94.8</b>	<b>87.7</b>	<b>90.0</b>	<b>97.8</b>
	WISE-FUSE	87.7	<b>88.4</b>	<b>90.6</b>	84.9	85.7	93.0	86.9	89.8	97.5

Table 10: Performance of cancer subtyping using MIL on TCGA-BRCA, TCGA-NSCLC, and TCGA-RCC. <sup>†</sup> denotes the variant without knowledge fusion (patch selection only).

Model	Method	TCGA-BRCA			TCGA-NSCLC			TCGA-COAD		
		ACC	W_F1	AUC	ACC	W_F1	AUC	ACC	W_F1	AUC
–	1.25× all	64.6	67.5	56.7	55.0	54.2	57.4	69.4	70.6	64.6
	20× all	62.2	67.8	58.5	57.6	56.5	62.4	66.1	68.6	66.5
	20× 10%	56.0	64.3	57.1	53.4	54.1	60.9	65.0	67.7	66.8
CONCH	WISE-FUSE <sup>†</sup>	<b>58.5</b>	<b>65.1</b>	<b>58.8</b>	<b>59.6</b>	<b>58.3</b>	<b>63.5</b>	<b>69.3</b>	<b>71.3</b>	<b>63.9</b>
	WISE-FUSE	46.8	51.6	49.8	55.8	55.5	61.6	69.1	68.4	63.2
PLIP	WISE-FUSE <sup>†</sup>	<b>62.1</b>	<b>67.0</b>	<b>60.0</b>	<b>58.3</b>	57.8	<b>61.9</b>	65.4	68.7	<b>65.7</b>
	WISE-FUSE	55.3	60.8	57.8	55.2	<b>58.5</b>	61.8	<b>67.3</b>	<b>70.9</b>	65.4
Biomed CLIP	WISE-FUSE <sup>†</sup>	60.1	67.6	58.7	57.2	57.1	<b>64.6</b>	68.4	70.3	<b>64.4</b>
	WISE-FUSE	<b>60.2</b>	<b>68.0</b>	<b>59.1</b>	<b>58.0</b>	<b>58.3</b>	64.3	<b>70.2</b>	<b>70.8</b>	63.7

Table 11: Performance of survival prediction using MIL on TCGA-BRCA, TCGA-NSCLC, and TCGA-COAD. <sup>†</sup> denotes the variant without knowledge fusion (patch selection only).

Model	Method	TCGA-BRCA (Molecular profiling)			TCGA-COAD (Metastasis prediction)			TCGA-STAD (Metastasis prediction)		
		ACC	W_F1	AUC	ACC	W_F1	AUC	ACC	W_F1	AUC
–	1.25× all	27.6	57.0	70.8	56.0	58.8	62.0	52.4	53.8	54.6
	20× all	32.1	60.2	76.1	52.5	54.7	58.5	58.1	57.5	69.2
	20× 10%	31.8	60.0	75.7	51.5	53.1	57.9	57.5	55.9	60.7
CONCH	WISE-FUSE <sup>†</sup>	26.5	58.8	73.8	<b>56.4</b>	<b>57.5</b>	<b>60.5</b>	<b>55.7</b>	51.2	<b>67.6</b>
	WISE-FUSE	<b>40.6</b>	<b>61.6</b>	<b>76.2</b>	55.8	56.8	59.3	49.9	<b>52.2</b>	52.2
PLIP	WISE-FUSE <sup>†</sup>	<b>35.2</b>	<b>59.4</b>	75.6	<b>53.5</b>	<b>53.1</b>	<b>59.4</b>	<b>62.6</b>	<b>56.0</b>	<b>73.1</b>
	WISE-FUSE	33.7	<b>59.4</b>	<b>76.3</b>	53.1	52.9	58.7	58.1	55.5	70.0
Biomed CLIP	WISE-FUSE <sup>†</sup>	31.4	57.9	74.7	<b>57.4</b>	<b>58.5</b>	<b>62.5</b>	<b>59.9</b>	<b>59.5</b>	<b>65.3</b>
	WISE-FUSE	<b>41.3</b>	<b>61.4</b>	<b>79.4</b>	55.3	57.3	61.9	58.8	58.5	64.6

Table 12: Performance of molecular profiling and metastasis prediction using MIL on TCGA-BRCA, TCGA-COAD, and TCGA-STAD. <sup>†</sup> denotes the variant without knowledge fusion (patch selection only).